Particle-in-cell simulations of current loss in magnetically insulated transmission line with inductive helical support

Wei Luo[1] , Yongdong Li[1], Hongguang Wang[1], Fan Guo[2], Wenkang Zou[2], Pengfei Zhang[3], Lei Zhang[1], Yu Gu[1] and Jianwei Zhang[1]

[1]Key Laboratory for Physical Electronics and Devices of the Ministry of Education, School of Electronic and Information Engineering, Xi'an Jiaotong University, Xi'an 710049, China; [2]Institute of Fluid Physics, China Academy of Engineering Physics, Mianyang 621900, China and [3]State Key Laboratory of Intense Pulse Radiation of Simulation and Effect, NINT, Xi'an 710024, China

Abstract

High inductive helical support provides a solution to controlling the alignment error of inner electrodes in magnetically insulated transmission lines (MITLs). Three-dimensional particle-in-cell simulations were performed to examine the current loss mechanism and the effects of structural parameters on electron flow in an MITL with a helical inductor. An empirical expression related to the ratio of electron current loss to anode current and the ratio of anode current to self-limited current was obtained. Electron current loss caused by helical inductor with different structures was displayed. The results indicate that the current loss in an MITL, near an inductive helical support, comprises both the inductor current and the electron current loss. The non-uniform structure and current of a helical inductor cause an abrupt change in the magnetic field near the helical support, which leads to anomalous behavior and current loss of electron flow. In addition, current loss in the inductive helical-supported MITL is negligible when the inductance of the support is sufficiently high. This work facilitates the estimation of electron current loss caused by the inductive helical support in MITLs.

CAMBRIDGE
UNIVERSITY PRESS

Introduction

Pulsed power-driven flash radiography uses a high-intensity pulsed electron beam to generate bremsstrahlung X rays as a probe for imaging hydrodynamic experiments (Smith 2004; Leckbee *et al.*, 2006; Guo *et al.*, 2019; Richardson *et al.*, 2019). In pulsed-power systems, such as Hermes-III (Renk *et al.*, 2014), URSA Minor (Pointon *et al.*, 2011), QiangGuang-1 (Wu *et al.*, 2011), the loads are always connected to the driver through the magnetically insulated transmission line (MITL). The MITL is an essential component in large pulsed power devices for guaranteeing the efficient transmission of high-power pulses (power density up to TW/cm^2) from driver to load (VanDevender *et al.*, 2015). When a high-power pulse propagates along the MITL, and electric field strength exceeds the threshold of explosive emission, electron emission will occur. The electron flow is accelerated to the anode and not magnetically insulated until the current is sufficiently high (Bruner *et al.*, 2008; Ottinger *et al.*, 2019).

In such high-power systems, the negative-polarity coaxial lines, a few to tens of meters in length (Luo *et al.*, 2017*a*), can be treated as MITLs. The upstream of the inner electrode in an MITL is usually fixed, while the end of the inner electrode is free of the support, which may cause misalignment of the inner electrode. Previous research with Hermes-III showed a noticeable current loss when the gap was misaligned by 25% (Burgess *et al.*, 1987). The misalignment can be mitigated; however, it is difficult to be eliminated in the experiments. Hence, a high inductive helical support provides a solution to controlling the alignment error of the inner electrode of the MITL (Zou *et al.*, 2012; Luo *et al.*, 2017*b*). In the region of the coaxial MITL with the helical support, the structure is non-uniform and the electromagnetic field is asymmetric. When electron flow enters a non-uniform MITL structure, it is disturbed by a non-uniform magnetic field and is not fully magnetically insulated (Bruner *et al.*, 2008, 2009; Leopold *et al.*, 2009; Zhang *et al.*, 2016; Luo *et al.*, 2019). Previous work has revealed that the inductive support causes a considerable current loss in the MITL when voltage is lower than 1 MV (Zou *et al.*, 2012). However, in a common pulsed power system for flash radiography, the peak voltage is up to several or tens of megavolts. The non-uniform structure and current of the helical inductor can cause an abrupt change in the magnetic field, and even current loss near the helical support. To improve the efficiency of the helical-supported MITL, the current loss mechanism and the effects of structural parameters of the helical inductor on electron flow need further investigation.

To investigate these issues, we performed particle-in-cell (PIC) simulations of a high inductive helical-supported MITL, with PIC codes-UNIPIC (Luo *et al.*, 2017*a*, 2017*b*; Wang *et al.*, 2018; Luo *et al.*, 2019). This paper is arranged as follows: section "Simulation setup" describes the simulation setup; the choice of structural parameters for the MITL and the helical support are analyzed; then, conditions of the PIC simulations of the helical-supported MITL are investigated. Section "Particle-in-cell results and analysis" presents the PIC simulation results and analysis of the MITL, supported by the helical inductor. The current loss caused by the shunt current of the inductor and the disturbed electron current is discussed. Moreover, the effects of structural parameters of the helical inductor on electron flow are investigated. Finally, section "Conclusion" presents the conclusion.

Simulation setup

To control serious current loss caused by explosive emission on the support of a helical spring, the interval between the wings of the helical spring should be large enough to keep the electric field on the spring lower than that of the explosive-emission threshold. Therefore, the length of the inductor, including the helical spring and the rods, should be long enough; however, it is difficult to make it stiff enough with an increasing length of the inductor. To control the length of the support, the helical spring can be directly connected to the cathode. Based on previous work (Zou *et al.*, 2012), a 3D model of the helical-supported MITL is shown in Figure 1. The MITLs with different structures of support are simulated with 3D PIC codes-UNIPIC, with Cartesian coordinates. The *z* direction is defined as the power flow direction. The support contains the helical spring and the metal rods. The hole and the outer cylinder surround the support. Arrangement of these components makes the MITL asymmetric. When pulsed power transmits through the region with helical support, the non-uniform structure will generate a non-uniform distribution of magnetic field and impedance of the MITL, and then the electron flow is perturbed and current loss may occur (Bruner *et al.*, 2008, 2009; Leopold *et al.*, 2009; Zou *et al.*, 2012; Zhang *et al.*, 2016; Luo *et al.*, 2017*b*, 2019).

The whole length of the MITL is 1.05 m, and the helical support is placed at $z = 0.5$ m, which is contained in a cylindrical tube. r_a and r_c are the inner radius of the anode and outer radius of the cathode, respectively. The MITL is terminated with a hollow diode, and the anode–cathode (AK) gap of the diode is displayed with coefficient *d*. The inductance of the helical inductor is $(\mu_0/4\pi)2RW^2\phi$, where u_0 is the permeability in vacuum, *W* is the number of windings of the inductor, *R* is the radius of the inductor, and *a* is the total length. Additionally, ϕ is a function of *a*/2*R* (Kalantarov and Tseitlin, 1986). The helical inductor is parallel to the load, so the shunt current in the inductor cannot be neglected. In the experiments, the maximum allowed current loss is 10% of the total current. The common rise time of pulsed power varies from 70 to 100 ns, so the frequency range is about 2.5–3.5 MHz. For the low impedance load, an equivalent impedance of more than 100 Ω for the support is necessary (Zou *et al.*, 2012). For benchmarking in the simulation model, the radius and length of the inductor are 5 and 12 cm, respectively, the number of wings is 25 (*L* then equals 26.5 μH), and the impedance almost equals 520 Ω.

The diameter of the tube covering the helical support is 15 cm, and the load of the MITL is a large area electron beam diode. The outer diameter and the inner diameter of the cathode in the diode
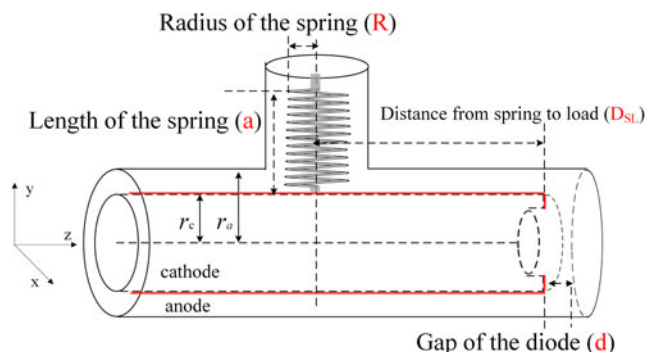

Fig. 1. Simulation model of high inductive helical-supported MITL.

are 11 and 8 cm, respectively. The anode-to-cathode (AK) gap of the diode, *d*, varies from 18 to 30 mm in some simulation cases. Explosive electron emissions begin on the diode cathode when the electric field exceeds 20 kV/cm, while the electron emission threshold for the MITL cathode is 200 kV/m. A uniform grid is applied in all directions. Grid sizes in the *x* and *y* directions are set as $dx = 3$ mm and $dy = 1.6$ mm, respectively. The grid size in *z* direction, *dz*, varies from 1.6 to 2 mm. The waveform of the input voltage is described by a sine function, and the rise time is 100 ns.

Particle-in-cell results and analysis

Current loss mechanism for helical-supported MITL

To analyze the current loss mechanism of the MITL caused by the helical inductor, PIC simulations of a helical inductive supported MITL, with varied diode impedance, were constructed. The total current loss caused by the helical support (I_a^{Loss}) consists of the shunt current in the inductor ($I_{inductor}$) and the electron current leaked to the anode from $z = 0.3$ m to $z = 0.7$ (I_e^{Loss}), which can be expressed as:

$$I_a^{Loss} = I_{inductor} + I_e^{Loss}. \tag{1}$$

The length and radius of the helical spring and the number of wings are 12, 5, and 25 cm, respectively. The inductance of the inductor is about 26.5 μH. Figure 2 shows the voltage and current waveforms of the helical-supported MITL when $d = 21$ mm. The peak voltage is 0.74 MV, while the peak current is 83.8 and 80.4 kA for I_{a1} and I_{a2}, respectively. Curves I_{a1} and I_{a2} represent the anode current before and after the inductor, respectively. The divergence between I_{a1} and I_{a2} indicates a considerable current loss when pulsed power transmits though the region with the inductor, which is shown in Figure 3. The total loss of 3.44 kA for the peak current is at 100 ns in Figure 3. The anode current before the inductor can be expressed as $I_{a1} = I_{a2} + I_e^{Loss} + I_{inductor}$. The electron current loss is about 1.04 kA at 100 ns, while the current in the inductor is 2.4 kA. The helical inductor generates a shunt current and non-uniform structure of the MITL. A non-uniform structure will cause an abrupt change in impedance and a non-uniform magnetic field, which can lead to electron current loss. To improve the efficiency of the helical-supported MITL, the current loss mechanism caused by the helical inductor needs further investigation.

To elucidate electron behavior in the helical-supported MITL described above, the distribution of electron flow is shown in Figure 4. Electron flow near the diode in the MITL is effectively
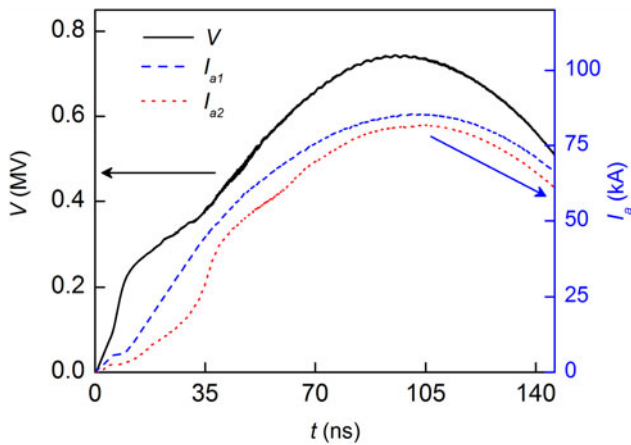
Fig. 2. Time histories of voltage and current for the helical-supported MITL with $d = 21$ mm. The inductance is 26.5 μH.
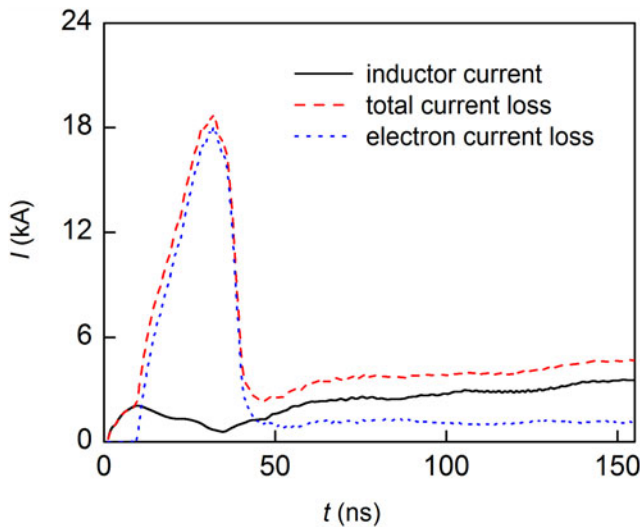
Fig. 3. Current loss of the helical-supported MITL with $d = 21$ mm. The inductance is 26.5 μH.

insulated in Figure 4a, while the electron layer after the helical support from 0.6 to 0.8 m is extended to the anode. This phenomenon may cause a substantial current loss after the helical inductor. The electron flow near the helical spring is disturbed, and a small part of the flow enters the outer cylinder. When the AK gap of the diode is decreased to 18 mm, the reflected wave from the load decreases the voltage and enhances the total current. Then, the electron layer is tightly confined to the cathode. Better magnetic insulation is achieved, and electron flow after the helical inductor is fully magnetically insulated. However, the flow is perturbed when entering the helical spring region. A proportion of electrons flows into the outer cylinder, especially in the region between the outer cylinder and helical spring, from about 0.42 to 0.45 m. The results indicate that electron flow leakage occurs, although the total current is sufficiently high in the helical-supported MITL.

To analyze the current loss mechanism in the MITL, the magnetic field distribution near the helical inductor in the *YZ* plane is displayed. Figure 5a shows the total magnetic field intensity, and Figure 5b and 5c are the magnitude of the magnetic fields in the *x* and *y* direction, respectively. Figure 5a reveals that the magnitude of the magnetic field before and after the helical support varies

from 0.08 to 0.16 T; the magnitude of the magnetic field near the helical spring is much higher. The spring field is produced by the spring itself, which agrees with the distribution of B_y in Figure 5c. The enhanced B_y component will disturb the electron flow near the spring and may cause current loss. Based on the theoretical model (Ottinger and Schumer, 2006), the critical magnetic field for magnetic insulation (B_{crit}) of the MITL in Figure 4a at 0.74 MV is about 0.096 T. Figure 5b indicates that the azimuthal magnetic field in the green region meets 0.05 T < B_x < 0.09 T, which means that the azimuthal magnetic field near the helical support is lower than B_{crit}. As Figure 4a shows, when electron flow enters the helical spring region, the weakened azimuthal magnetic field cannot confine the electron flow effectively. This results in a proportion of the electrons flowing into the outer cylinder. The azimuthal magnetic field near the cathode also decreases after the helical support. As a result, the electron layer after the helical support is close to the anode.

Total intensity of the magnetic field is enhanced near the spring, especially the red regions inside the spring in Figure 6a. Distribution of the azimuthal magnetic field in Figure 6b reveals that B_x, near the left part of helical spring, becomes negative, in contrast with the positive values when $y > 0$. Then, negative B_x deflects electron flow to the anode via the Lorenz force, which agrees with the electron behavior in Figure 7b. Figure 6c shows that B_y is negative inside the spring region and positive outside it. Negative B_y will deflect the electron flow in the positive *x* direction, while positive B_y will deflect it in the negative *x* direction. On the left side of the helical spring in Figure 7b, negative B_x deflects electron flow to the anode while positive B_y deflects it in the negative *x* direction. As a result, the electron flow is disturbed and enters the outer cylinder which surrounds the helical spring.

The electron distributions in the helical-supported MITLs, with a 21 mm-gap diode and an 18 mm-gap diode, in the *XY* plane in Figure 4, are shown in Figure 7. The electron layer is almost uniform at $z = 0.3$ m, when the AK gap of the diode is 21 or 18 mm. When $z = 0.5$ m, the electron flow is disturbed and some electrons run away from the MITL to the outer cylinder. It is clear that fewer electrons enter the outer cylinder when $d = 18$ mm, which results in a higher total current. Snapshots of electrons at $z = 0.7$ m in Figure 7c and 7f show that the electron flow does not leak to the anode with higher current.

In Figure 8, as electrons are lost to the anode near the helical support before 100 ns, the electron current I_e at $z = 0.5$ m is smaller when compared with I_e at $z = 0.3$ m. When the anode current increases and reaches peak value at 100 ns, the magnetic insulation of electrons at 0.3 m $\leq z \leq 0.5$ m is enhanced, and the electrons are mainly lost to the anode after $z > 0.5$ m, which is shown in Figures 4a and 7c. Therefore, I_e at $z = 0.3$ m is nearly equal to that at $z = 0.5$ m after 100 ns. Figure 9 shows the plots of I_e^{Loss}/I_a as functions of I_a/I_a^{SL}, where I_e^{Loss}, I_a, and I_a^{SL} are the electron current loss near the support (0.3 m < z < 0. 7 m), anode current after the support, and self-limited current of the MITL, respectively. When I_a/I_a^{SL} equals 1, the MITL operates at self-limited flow, and I_e^{Loss}/I_a achieves the maximum value of about 2% with 0.7 and 4.9 MV. An empirical expression can be obtained by fitting the curves of 0.74 and 4.9 MV:

$$I_e^{\text{Loss}}/I_a = 0.2 - 0.285(I_a/I_a^{\text{SL}}) + 0.103(I_a/I_a^{\text{SL}})^2. \qquad (2)$$

When I_a/I_a^{SL} increases from 1 to 1.4, the MITL operates from self-limited flow to load limited flow, and higher anode current provides a stronger azimuthal magnetic field to confine the
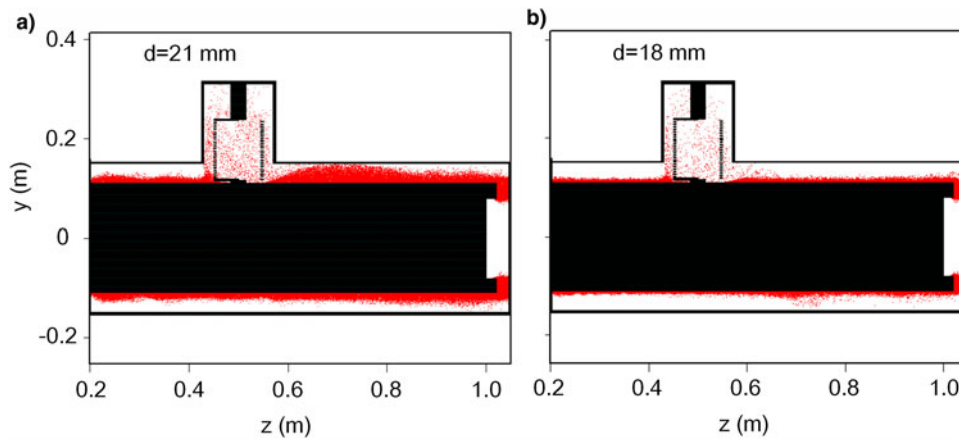
Fig. 4. Snapshots of electrons in the MITL in the *YZ* plane at 100 ns. *d* is 21 mm in (a) and 18 mm in (b). The inductance is 26.5 μH.
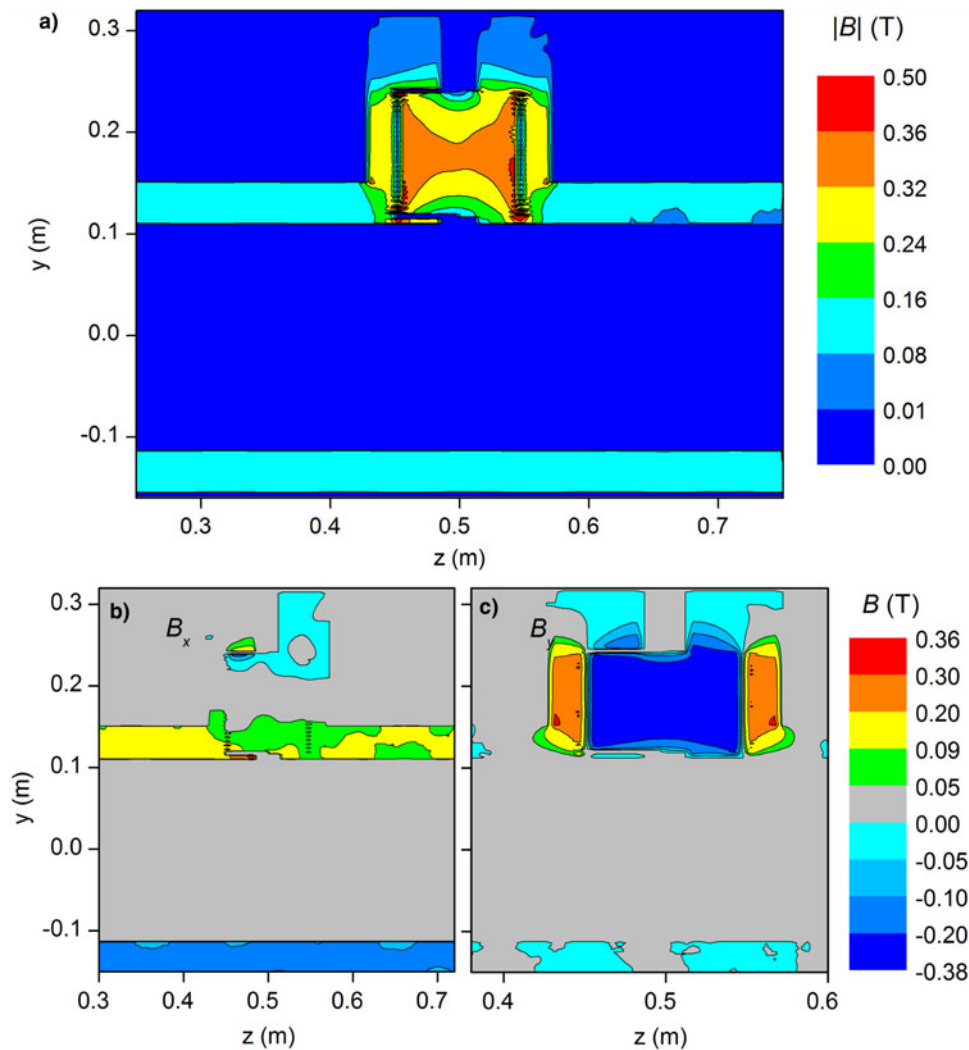

Fig. 5. Magnitude of magnetic fields of (a) absolute value, (b) B_x, and (c) B_y in the MITL of Figure 4a in the *YZ* plane at 100 ns, *d* = 21 mm.

electron flow, as a result, smaller current loss occurs. To make sure I_e^{Loss}/I_a is less than 0.5%, I_a/I_a^{SL} should be no less than 1.3. For a simple calculation, we assume:

$$I_{a\,sup}^{SL} = I_a^{SL} + I_e^{Loss} \qquad (3)$$

where $I_{a\,sup}^{SL}$ is the total current of the MITL in a self-limited case before the support minus the inductor current.

As the helical inductor causes a shunt current and electron current loss, varied inductance of the helical inductor may cause different current loss. As the electron current loss reaches
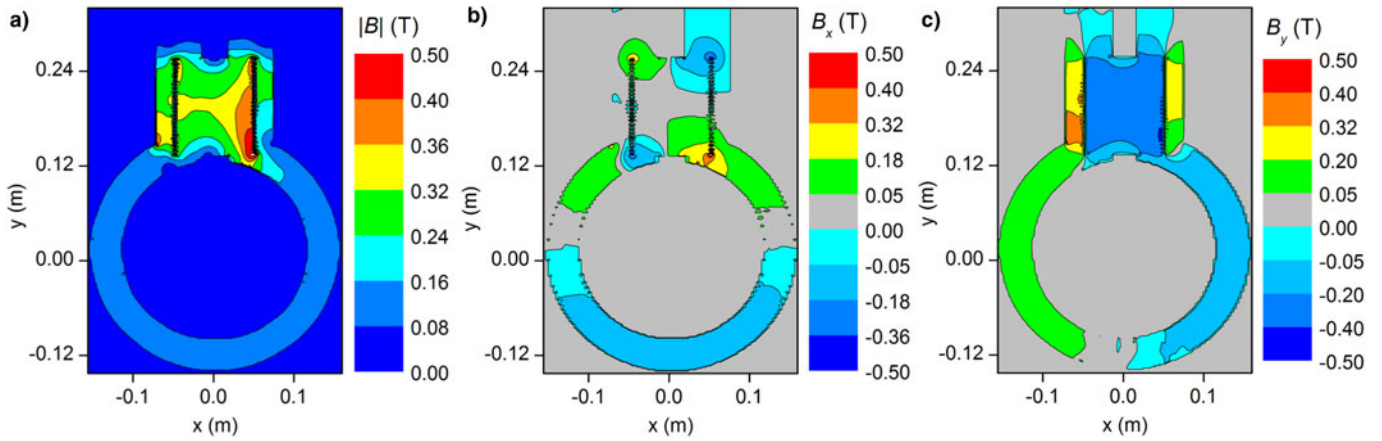
Fig. 6. Magnitude of magnetic fields of (a) absolute value, (b) B_x, and (c) B_y in the MITL of Figure 4a in the *XY* plane at 100 ns, $d = 21$ mm.
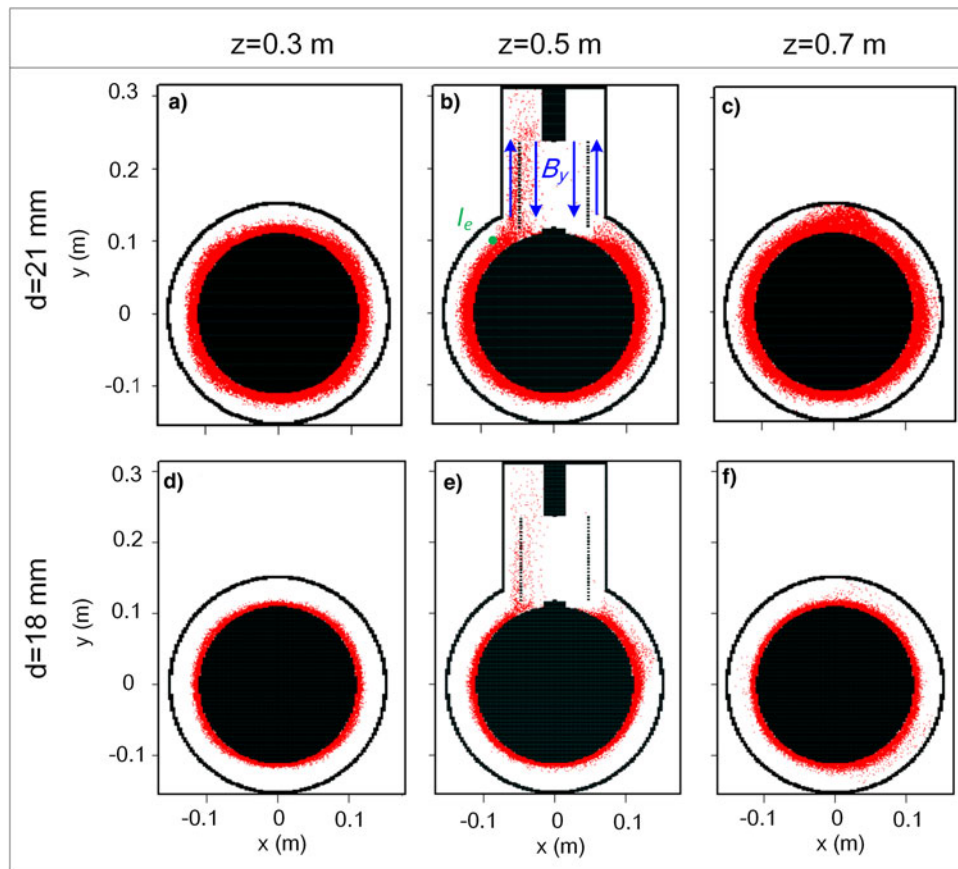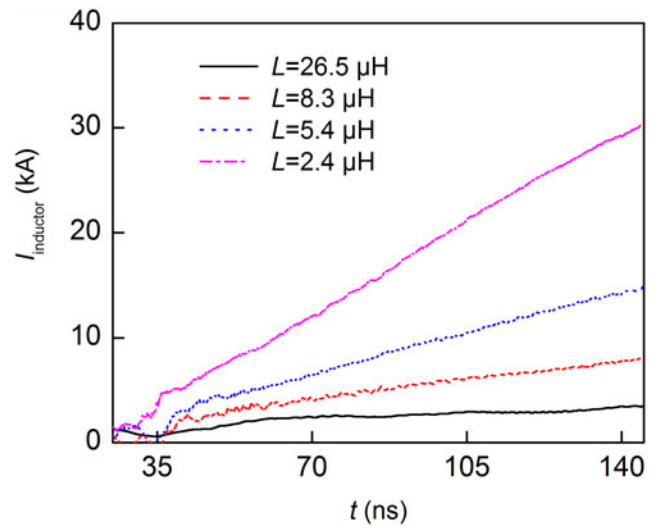

Fig. 7. Snapshots of electrons in the MITL of Figure 4 in the *XY* plane at 100 ns. (a), (b), and (c) describe the particle plots at cross-sections of $z = 0.3$ m, $z = 0.5$ m, and $z = 0.7$ m when $d = 21$ mm, respectively. (d), (e), and (f) describe the particle plots at cross-sections of $z = 0.3$ m, $z = 0.5$ m, and $z = 0.7$ m when $d = 18$ mm, respectively.

the maximum value, when the helical-supported MITL operates in the self-limited case, the MITL operates in the self-limited case. Figures 10 and 11 show the inductor current and the electron current loss for the helical-supported MITL with varied inductance. The inductor current at 100 ns is about 2.6, 5.7, 9, and 22.4 kA for inductances of 26.5 μH, 8.3, 5.4, and 2.4 μH, respectively. The electron current loss near the helical inductor at 100 ns is about 1.4, 1.6, 2.3, and 3.2 kA for inductances of 26.5, 8.3, 5.4, and 2.4 μH, respectively. The results indicate that the electron current loss is far less than the shunt current by
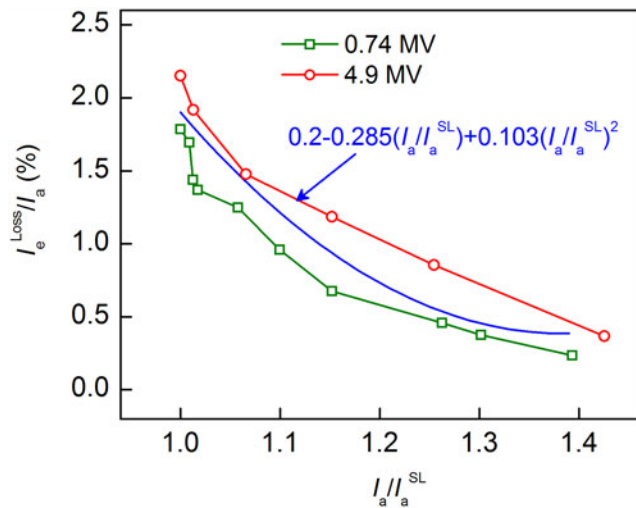
the inductor. The helical-supported MITL, with different inductors, is operated in the self-limited case. The peak anode current after the inductor in these MITLs is equal. Next, the different electron loss near the helical support is analyzed. Figure 12a and 12b show the distribution of electrons in the MITL with helical inductors of 26.5 and 2.4 μH, respectively. The structure of the MITL in Figure 10a is the same as that in Figure 4. Results in Figure 12a and 12b reveal that the downside electron flow keeps magnetic insulation when $z > 0.7$ m; however, the upside electrons are lost to the anode when $z > 0.7$ m. In Figure 12b, more electrons
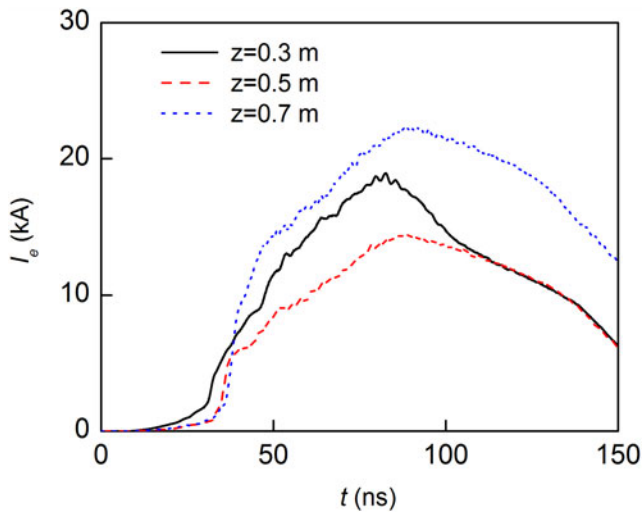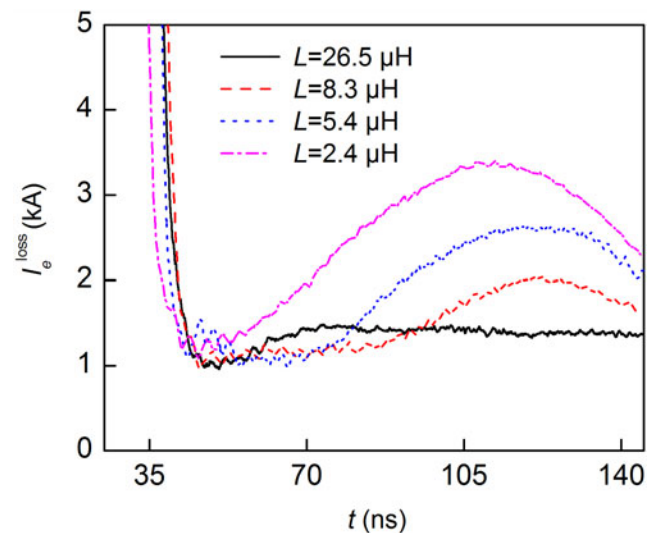
Fig. 8. Electron current for the MITL in Figure 4a at different positions in the *z* direction.


Fig. 9. Plots of I_e^{Loss}/I_a as functions of I_a/I_a^{SL} for simulation results (labeled 0.72 and 4.9 MV) and fitting results. I_e^{Loss}, I_a, and I_a^{SL} are the electron current loss near the support (0.3 m < *z* < 0. 7 m), anode current after the support, self-limited current of the MITL, respectively.

Fig. 10. Inductor current for the helical-supported MITL in the self-limited case. The peak voltage is 0.74 MV.

Fig. 11. Electron current loss for the helical-supported MITL in the self-limited case in Figure 10.
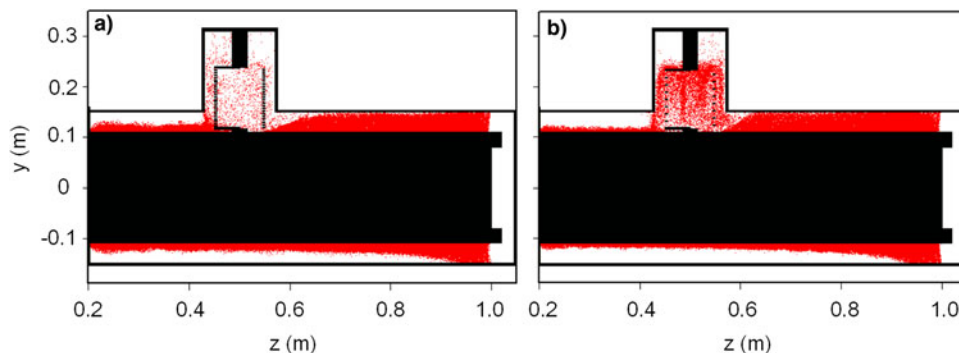
Fig. 12. Snapshots of electrons in the MITLs with different inductances in the *YZ* plane at 100 ns. The MITLs are operated in the self-limited case. The inductance of helical inductors in (a) and (b) are 26.5 and 2.4 μH, respectively.
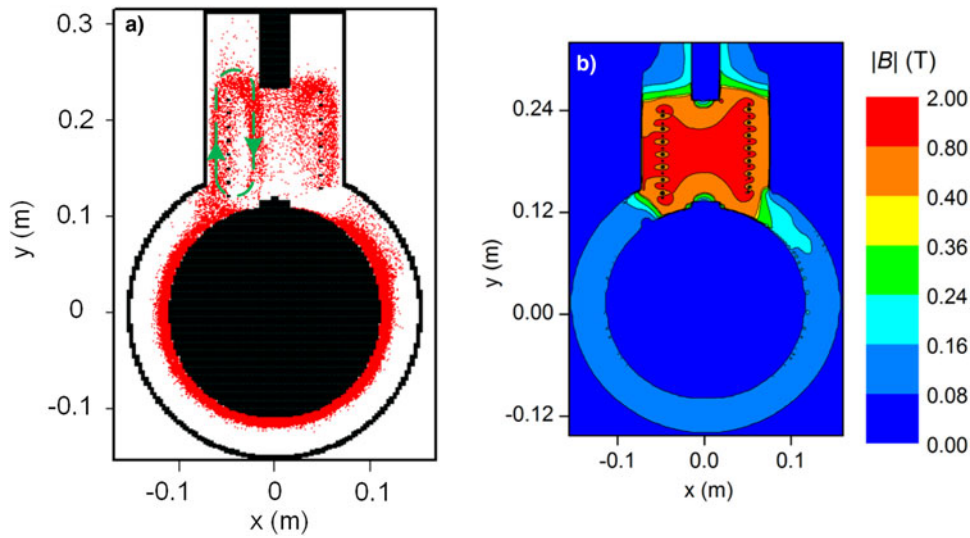
Fig. 13. Snapshots of (a) electrons and (b) the magnitudes of magnetic fields in the MITLs in Figure 12b in the *XY* plane at 100 ns.
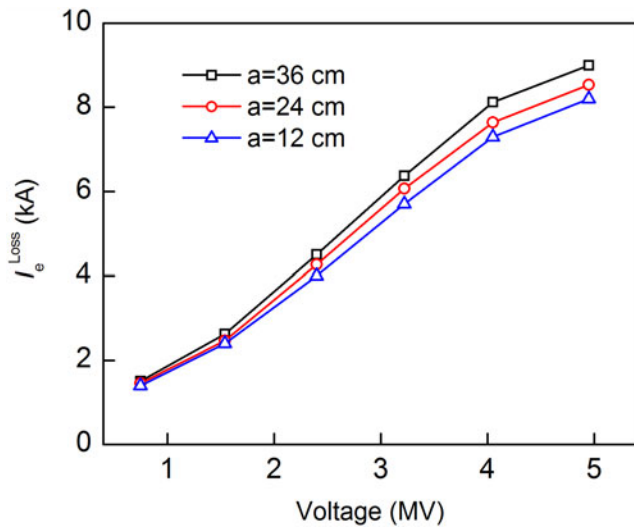

Fig. 14. Electron current loss versus voltage for MITLs in the self-limited case. The lengths of the helical spring are 12, 24, and 36 cm. The interval between the wings of the helical inductor varies from 4.8 to 9.6 mm.
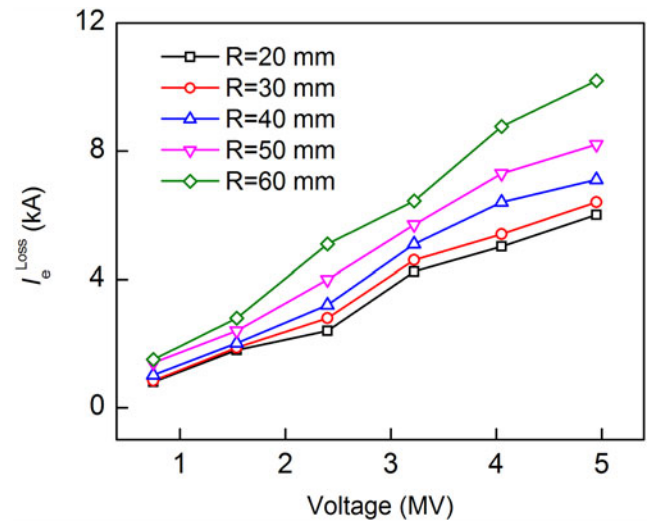
Fig. 15. Electron current loss versus voltage for MITLs of geometry 3 in the self-limited case. The radius of the helical inductor varies from 20 to 60 mm.

enter the outer cylinder surrounding the helical spring than that in Figure 12a and cause higher current loss. However, the electron flow before the helical inductor in Figure 12b is more tightly confined to the cathode due to a higher total current with a smaller inductance.

It is clear that a smaller inductance causes a much higher magnetic field in the *y* direction, which is shown in the red region of Figure 13b. This field is much higher than the azimuthal magnetic field near the helical spring, which generates an electron flow vortex near the spring, shown in Figure 13a.

Effects of structural parameters of the helical inductor on electron current loss of MITL

To investigate the effects of structural parameters of the helical spring on electron current loss, simulations of helical-supported MITLs with different springs were conducted. The inductance

was fixed at 26.5 μH, as is the case for the inductor in Figure 4. For the helical spring of the MITL in simulations of Figure 14, R is set as 5 cm, to obtain a fixed inductance at 26.5 μH when a ranges from 12 to 36 cm, a/W varies from 4.8 to 9.6 mm according to the equation of inductance in "Simulation setup". Results show that the electron current loss caused by the helical spring changes slightly with the length and the number of wings of the spring when the inductance of the spring is fixed. In Figure 15, a/W is set as 4.8 mm, when R varies from 20 to 60 mm, a varies from 10 to 30 cm to obtain a fixed inductance. Results reveal that a larger helical spring radius causes a higher electron loss in the MITL. The difference between the electron current loss of the larger-radius spring and that of the smaller-radius spring may be caused by the non-uniform distribution of the magnetic field. Therefore, a trade-off between a large electron current loss caused by a large-radius helical spring and the difficulty of support for a small-radius helical spring is required.
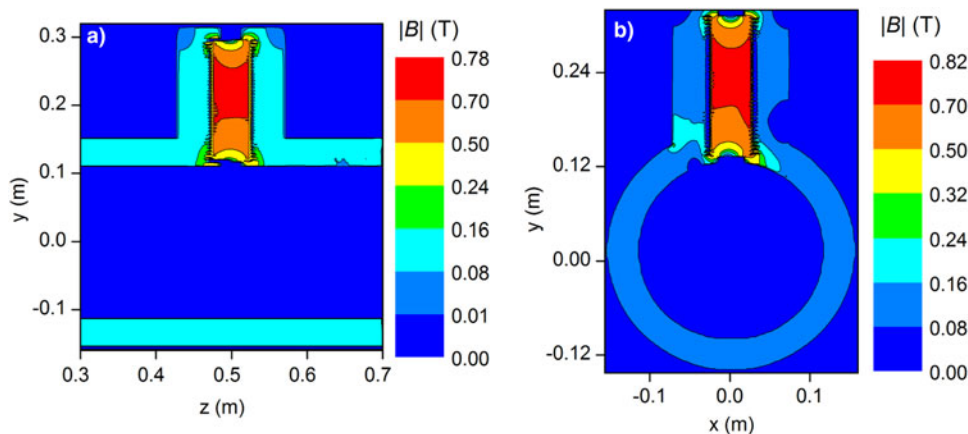
Fig. 16. Magnetic fields of MITLs at the center of the inductor in the (a) *YZ* plane and (b) *XY* plane at 100 ns. The MITL is operated in the self-limited case. *V* = 0.74 MV.
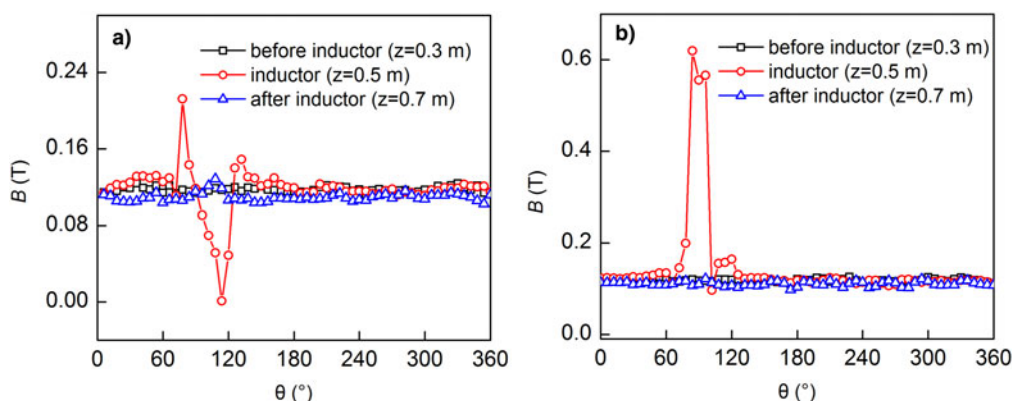

Fig. 17. Magnetic fields of MITLs with (a) 5 cm-radius and (b) 3 cm-radius inductor at 100 ns. The MITL is operated in the self-limited case.
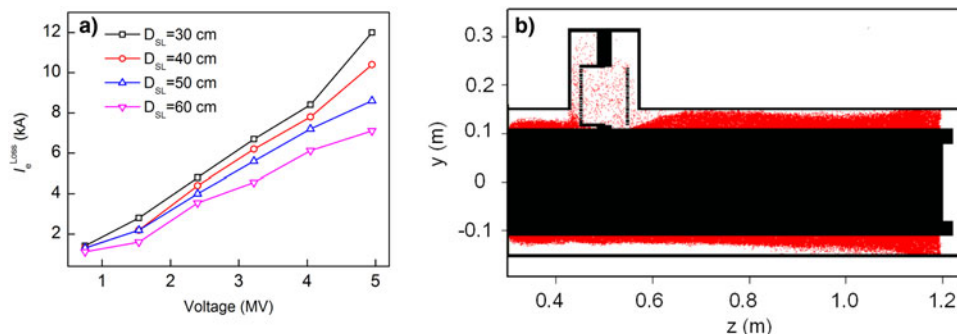

Fig. 18. Electron current loss versus voltage for MITLs in the self-limited case, with different distances from the helical support to the load in (a) and snapshots of electrons in MITL when D_{SL} is 70 cm in (b). The helical spring is the same as that in Figure 4.

As Figure 16 shows, the magnetic field near the outer cylinder is not disturbed in the MITL with the 3 cm-radius inductor, in contrast with the field of the MITL with the 5 cm-radius inductor, in Figure 5a. The results in Figure 17 show that the magnetic field before the inductor is uniform and it is beyond the critical magnetic field (B_{crit} = 0.097 T). However, the magnetic field at the center of the inductor becomes non-uniform and exits abrupt changes from 60° to 120° along the angular path. After the inductor, the magnetic field fluctuations decrease, the average value of the intensity of the magnetic field after the inductor is about 91.5% of that before the inductor in Figure 17a and 93.2% of that in Figure 17b. The magnetic

field near the helical spring of the MITL with the 3 cm-radius inductor is always higher than 0.096 T, which leads to a lower electron current loss.

As the helical support impacts the local magnetic field, when pulsed power propagates in the MITL, it is clear that the support will disturb electron flow and the working property of the load. Figure 18a shows current loss with distance from the helical support to the load, from 30 to 60 cm. The helical inductor is the same as that in Figure 4. As the distance from the support to the load increases, a smaller electron current is lost to the anode wall of the MITL. In the self-limited case of magnetic insulation for the MITL, a large distance between the support
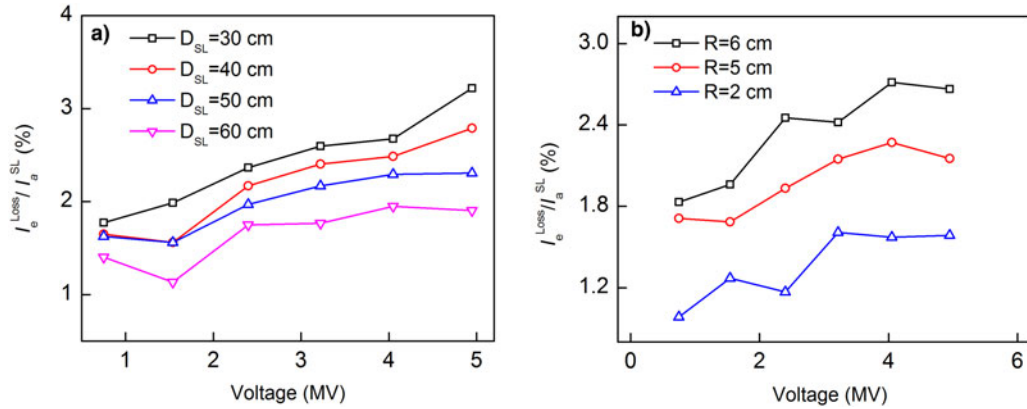
Fig. 19. Plots of I_e^{Loss}/I_a^{SL} as functions of operating voltage of the MITL with varied (a) distance from support to the load and (b) radius of helical spring. The inductance of the helical spring is 26.5 μH.

and the load means that the loss front is far from the helical support. Therefore, the electron flow of the MITL near the support is influenced only slightly. The snapshot of electrons in Figure 18b shows that the electron flow in the MITL is interrupted, becoming non-uniform again after the helical support. However, electron flow becomes uniform when the distance is larger than 40 cm.

As Figure 19a shows, the ratio of electron current loss to self-limited current, I_e^{Loss}/I_a^{SL}, is as high as 3.22% when $D_{SL} = 30$ cm at 5 MV, and is about 2.78% when $D_{SL} = 30$ cm at 5 MV. To make I_e^{Loss}/I_a^{SL} in the MITL less than 3% when the voltage varies from 0.5 to 5 MV, the distance from the spring to the load exceeding 0.4 m is an appropriate option. In Figure 19b, the ratio of electron current loss to self-limited current I_e^{Loss}/I_a^{SL} for MITLs with springs of various radii changes from 1 to 2.6%. The inductance and structure of the inductor are the same as those in Figure 4. When the inductance of the helical inductor is 26.5 μH, the ratio of shunt current to total current is about 3%, which is higher than I_e^{Loss}/I_a^{SL} at low voltage. If the inductance is sufficiently high, the electron current loss and inductor current are negligible when compared with the total current.
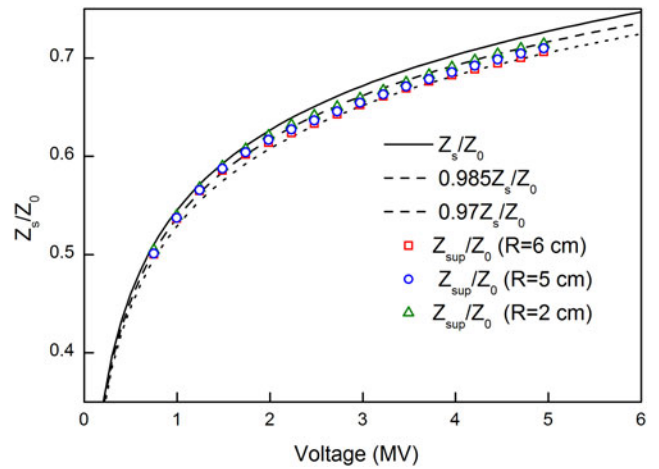
The self-limited impedance of the MITL is defined as $Z_S = V/I_a^{SL}$, which of the MITL with 26.5 μH inductor is compared with the theoretical model (Ottinger and Schumer, 2006) in Figure 20. I_a^{SL} for the theoretical model can be calculated though:

$$I_a^{SL}(V) = \frac{V}{Z_0 f_{SL}(V)} \left[\frac{1 + (((g(V)mc^2)/2eV) - 1)f_{SL}(V)}{1 - f_{SL}(V)} \right]^{1/2}, \quad (4)$$

$$f_{SL}(V) = \eta(V)f_{MC}(V), \quad (5)$$

where V and Z_0 are the operating voltage and vacuum impedance of the MITL, respectively. e, m, and c are the electron charge,

Fig. 20. Self-limited impedance as a function of voltage for MITLs with varied-radius springs. The inductance of the helical spring is 26.5 μH.

electron mass, and the speed of light, respectively. $g(V) = 0.99565 - 0.05332V + 0.0037V^2$, $\eta(V) = 0.82 + 0.0086V$. The self-limited impedance of the MITL near the inductive helical support is $Z_{sup} = V/I_{a\,sup}^{SL}$. Results in Figure 20 reveal that Z_{sup}/Z_0 of the MITL with a 6 cm-radius spring is about 0.97 times of the theoretical value, while Z_{sup}/Z_0 of the MITL with a 2 cm-radius spring is about 0.985 times of Z_S/Z_0.

Conclusion

In this paper, the current loss mechanism for an MITL supported with a helical inductor is discussed, and the effects of structural

$$f_{MC}(V) = \frac{((g(V)mc^2/8eV) - 1) + [((g(V)mc^2/8eV) - 1)^2 + ((g(V)mc^2/2eV) - 1)]^{1/2}}{((g(V)mc^2/2eV) - 1)}, \quad (6)$$

where V and Z_0 are the operating voltage and vacuum impedance of the MITL, respectively. e, m, and c are the electron charge,

parameters of the inductor on electron flow were investigated using 3D PIC simulations. Results reveal that the current loss

consists of the shunt current from the inductor and the electron current lost to the anode. The electron current loss reaches its maximum value when the helical-supported MITL is self-limited. The weakened azimuthal magnetic field near the helical spring prevents full magnetic insulation of the electron flow, and the flow is lost to the anode. The magnetic field produced by a small-inductance helical spring perturbs the electron flow and promotes electron current loss. An empirical expression for the ratio of electron current loss to anode current (I_e^{Loss}/I_a) as a function of the ratio of anode current to self-limited current (I_a/I_a^{SL}) is obtained. To ensure I_e^{Loss}/I_a is less than 0.5%, I_a/I_a^{SL} should be no less than 1.3.

Effects of helical inductors with different structures on electron flow were investigated when the inductance is fixed. The simulations are run using various voltage amplitudes. The radius of the helical spring is the key structural parameter which influences electron flow. To regain uniformity of the disturbed electron flow after the support and to achieve a I_e^{Loss}/I_a^{SL} less than 3%, the distance from the spring to the load should exceed 0.4 m. I_e^{Loss}/I_a varies from about 1 to 2.6% for the MITL with the 26.5 µH inductor, which indicates that the current loss of the inductive helical-supported MITL is negligible, when the inductance of the support is sufficiently high. This work addresses several important challenges associated with power flow in the inductive helical-supported MITL, and provides a simple solution to estimating the electron current loss caused by the inductive helical support.

References

Bruner N, Genoni T, Madrid E, Rose D, Welch D, Hahn K, Leckbee J, Portillo S, Oliver B, Bailey V and Johnson D (2008) Modeling particle emission and power flow in pulsed-power driven, nonuniform transmission lines. *Physical Review Special Topics – Accelerators and Beams* **11**, 040401.

Bruner N, Genoni T, Madrid E, Welch D, Hahn K and Oliver B (2009) Excitation of voltage oscillations in an induction voltage adder. *Physical Review Special Topics – Accelerators and Beams* **12**, 070401.

Burgess EL, Crowder GW, Dowdican MC, Patterson JC, Franklin TL, Robischon SJ, Tolk KM, Ramirez JJ, Johnson DL and Pate RC (1987) Alignment of the hermes-III magnetically insulated transmission line. *Proceedings of the 6th IEEE International Pulsed Power Conference, Arlington, VA*, pp. 506–509.

Guo F, Xie WP, Wang Z, Jiang JH, Xia MH, Wei B, Feng SP, Zhao Y, Kang JJ, Wang M, Zou W and Chen L (2019) Design of a 1-MV induction cavity and validation of the two-dimensional circuit model. *Physical Review Accelerators and Beams* **22**, 020401.

Kalantarov PL and Tseitlin LA (1986) *Inductance Calculation Manuals*. Leningrad, Soviet Union: The Atomic Energy Press.

Leckbee JJ, Maenchen JE, Johnson DL, Portillo S, Vandevalde DM, Rose DV and Oliver BV (2006) Design, simulation, and fault analysis of a 6.5-MV LTD for flash X-ray radiography. *IEEE Transactions on Plasma Science* **34**, 1888.

Leopold JG, Gad R, Leibovitz C and Navon I (2009) Numerical experiments on matching vacuum transmission lines to loads. *IEEE Transactions on Plasma Science* **37**, 50.

Luo W, Wang H, Li Y and Han Q (2017*a*) Properties of loss front in long magnetically insulated transmission lines. *IEEE Transactions on Plasma Science* **45**, 997.

Luo W, Wang H, Li Y and Pen M (2017*b*) Circuit-PIC coupled model of 3D simulation for magnetically insulated transmission line system. *In 2017 IEEE 21st International Conference on Pulsed Power*. IEEE.

Luo W, Li Y, Wang H, Liu C, Guo F, Zhang L, Gu Y and Zhang J (2019) Magnetic insulation in a curved vacuum transmission line. *Journal of Applied Physics* **125**, 163302.

Ottinger PF and Schumer JW (2006) Rescaling of equilibrium magnetically insulated flow theory based on results from particle-in-cell simulations. *Physics of Plasmas* **13**, 063109.

Ottinger PF, Renk TJ and Schumer JW (2019) Method for improved voltage determination for pulsed power systems utilizing a magnetically insulated transmission line. *Physics of Plasmas* **26**, 023105.

Pointon TD, Seidel DB, Leckbee JJ and Oliver BV (2011) PIC simulations of power flow in a linear transformer driver for radiographic applications. *Proceedings of the 15th IEEE International Pulsed Power Conference, Chicago, IL*, pp. 861–866.

Renk TJ, Harper-Slaboszewicz V, Mikkelson KA, Ginn WC, Ottinger PF and Schumer JW (2014) Use of a radial self-field diode geometry for intense pulsed ion beam generation at 6 MeV on Hermes III. *Physics of Plasmas* **21**, 123114.

Richardson AS, Zier JC, Engelbrecht JT, Swanekamp SB, Schumer JW, Mosher D, Ottinger PF, Duke DL, Haines TJ, McCumber MP and Gehring A (2019) Simulations of the generation and transport of a 5 MV end-point x-ray beam on a pulsed power generator. *Physical Review Special Topics – Accelerators and Beams* **22**, 050401.

Smith ID (2004) Induction voltage adders and the induction accelerator family. *Physical Review Special Topics – Accelerators and Beams* **7**, 64801.

VanDevender JP, Pointon TD, Seidel DB, Struve KW, Jennings C, Oliver BV and Schneider LX (2015) Requirements for self-magnetically insulated transmission lines. *Physical Review Special Topics – Accelerators and Beams* **18**, 030401.

Wang H, Zhang J, Li Y, Lin S, Zhong P and Liu C (2018) 2D particle-in-cell simulation of the entire process of surface flashover on insulator in vacuum. *Physics of Plasmas* **25**, 043522.

Wu J, Wang L, Qiu A, Han J, Li M, Lei T, Cong P, Qiu M, Yang H and Lv M (2011) Experimental investigations of X-pinch backlighters on QiangGuang-1 generator. *Laser and Particle Beams* **29**, 155–160.

Zhang P, Yang H, Sun J, Hu Y, Lai D, Li Y, Cong P and Qiu AC (2016) Experimental study on the current transmission efficiency for the transition structure of vacuum transmission line MITL on flash-II accelerator. *IEEE Transactions on Plasma Science* **44**, 1902.

Zou WK, Chen L, Liu DG, Zhang L, Liu LQ, Zhou LJ, Wang M, Wei B, Guo F, Wang XQ, Dai YM, Xie WP and Deng JJ (2012) Investigation on high inductive helical supported magnetically insulated transmission line on a 10-stage linear transformer driver system. *Physical Review Accelerators and Beams* **15**, 110401.